

Magnetization-driven Lifshitz transition and charge-spin coupling in the kagome metal YMn_6Sn_6

Peter E. Siegfried ^{1,2✉}, Hari Bhandari^{1,2}, David C. Jones^{1,2}, Madhav P. Ghimire^{3,4}, Rebecca L. Dally ⁵, Lekh Poudel ^{5,6}, Markus Bleuel^{5,6}, Jeffrey W. Lynn ⁵, Igor I. Mazin ^{1,2} & Nirmal J. Ghimire ^{1,2✉}

The Fermi surface (FS) is essential for understanding the properties of metals. It can change under both conventional symmetry-breaking phase transitions and Lifshitz transitions (LTs), where the FS, but not the crystal symmetry, changes abruptly. Magnetic phase transitions involving uniformly rotating spin textures are conventional in nature, requiring strong spin-orbit coupling (SOC) to influence the FS topology and generate measurable properties. LTs driven by a continuously varying magnetization are rarely discussed. Here we present two such manifestations in the magnetotransport of the kagome magnet YMn_6Sn_6 : one caused by changes in the magnetic structure and another by a magnetization-driven LT. The former yields a 10% magnetoresistance enhancement without a strong SOC, while the latter a 45% reduction in the resistivity. These phenomena offer a unique view into the interplay of magnetism and electronic topology, and for understanding the rare-earth counterparts, such as TbMn_6Sn_6 , recently shown to harbor correlated topological physics.

¹Department of Physics and Astronomy, George Mason University, Fairfax, VA 22030, USA. ²Quantum Science and Engineering Center, George Mason University, Fairfax, VA 22030, USA. ³Central Department of Physics, Tribhuvan University, Kirtipur, Kathmandu 44613, Nepal. ⁴Leibniz Institute for Solid State and Materials Research, IFW Dresden, Helmholtzstr. 20, D-01069 Dresden, Germany. ⁵NIST Center for Neutron Research, National Institute of Standards and Technology, Gaithersburg, MD 20899, USA. ⁶Department of Materials Science and Engineering, University of Maryland, College Park, MD 20742, USA. ✉email: psiegfri@gmu.edu; nghimire@gmu.edu

Conventionally, a phase transition is marked by the onset of an order parameter due to a spontaneously broken symmetry. Typically the order parameter is related to some thermodynamic quantity, e.g. magnetization, density, or polarization, that grows continuously after the transition. A Lifshitz transition (LT), on the other hand, is a unique electronic transition in metals associated with a change in the Fermi surface (FS) topology¹ that occurs without breaking any symmetries, and as such, LTs driven by a continuously changing magnetization are quite rare. The effect, however, is enhanced with the lowering of the effective dimension of the FS pocket involved and can play an important role in stabilizing new types of topological phases^{2–4}. In contrast, conventional field induced transitions concerning changes in magnetic texture (1st or 2nd order) involve a uniform rotation in spin space. Their effect on the electronic structure, and therefore on the transport properties, is controlled solely through the relativistic spin-orbit interaction, which is weak, determined by the fine structure constant $\alpha \simeq 1/137$, but grows with atomic number, Z . Typically a strong spin-orbit coupling (SOC) is required to observe magnetotransport signatures in this case. Here we show that the kagome lattice magnet YMn_6Sn_6 is a prototype system in terms of electronic transport that shows the two above mentioned magnetotransport properties. First, it exhibits a magnetization driven LT, with a strong effect on the c -axis conductivity, and second, a sizable electron-spin coupling without a strong SOC.

Results and discussion

Magnetization and magnetic structure. YMn_6Sn_6 is a ternary kagome magnet, a family of materials known to host a variety of topological states and phenomena^{5–8}. It crystallizes in the hexagonal space group $P6/mmm$ (#191)⁹ with Mn atoms forming a kagome net in the basal plane as depicted in Fig. 1a and b. The material orders antiferromagnetically at 340 K and quickly transitions into an incommensurate spiral below 333 K. At all temperatures, a magnetic field applied along the c -axis cants the moments lying in the ab -plane towards the c -axis, while for a magnetic field applied in the ab -plane, a series of competing phases^{10–12} are formed, as depicted in Fig. 1c (see Supplementary Note 2 for details). A schematic plot of the different magnetic

structures and their wavevectors is shown in Fig. 1d. Application of a magnetic field in the ab -plane first cants the spins rotating in the ab -plane, creating a distorted spiral phase, characterized by the wavevector $k = (0, 0, 0.26)$. When the magnetic field reaches H_1 , the spins flop to the perpendicular plane and cant towards the direction of the external field, maintaining the incommensurate c -axis spiral with only a slight increase in the spiral wavevector ($k_z = 0.27$). This phase is a transverse conical spiral. When the field reaches H_2 , the spins flop back into the ab -plane forming a commensurate fan-like phase. A projection of the fan-like spins onto the direction of the magnetic field (x -component) and along the perpendicular direction in the ab -plane results in a spin pattern repeating every two and four unit cells, respectively (see Supplementary Fig. 3), producing two different commensurate Bragg peaks observed in neutron diffraction at $k_z = 0.5$ and 0.25 , as shown schematically by the red lines in Fig. 1d. At H_3 the moments saturate to form the forced ferromagnetic phase.

Magnetotransport. Magnetoresistance (MR) at 1.8 K is plotted on the left axes of Fig. 2a and b. To compare the MR with the underlying magnetism, corresponding magnetization data are plotted in each figure on the right axis (see Supplementary Note 3 for the sensitivity of resistivity to the magnetic ordering with temperature). For the field applied in the ab -plane presented in panel (a), magnetization (black) shows a spin-flop transition at 2.2 T (H_1) corresponding to the distorted spiral - transverse conical spiral phase transition and a slope change slightly above 6.5 T (H_2) where the transverse conical spiral - fan like phase transition occurs. When current is applied in the ab -plane (MR_{ab}) (blue), the MR shows a small jump at 2.2 T (H_1), a small slope change at 4.5 T, and a sharp drop quickly above 8 T. The decrease in MR_{ab} above 8 T can be understood as polarization of the fan-like spins in the direction of the magnetic field, reducing spin fluctuations and the electron scattering. The slope change at 4.5 T has no corresponding change in the magnetization and is a small feature in this measurement configuration. In contrast, the MR with current along c (MR_c) (red) shows three remarkable features. First, there is no noticeable jump at H_1 despite the magnetic phase transition with a significant increase in

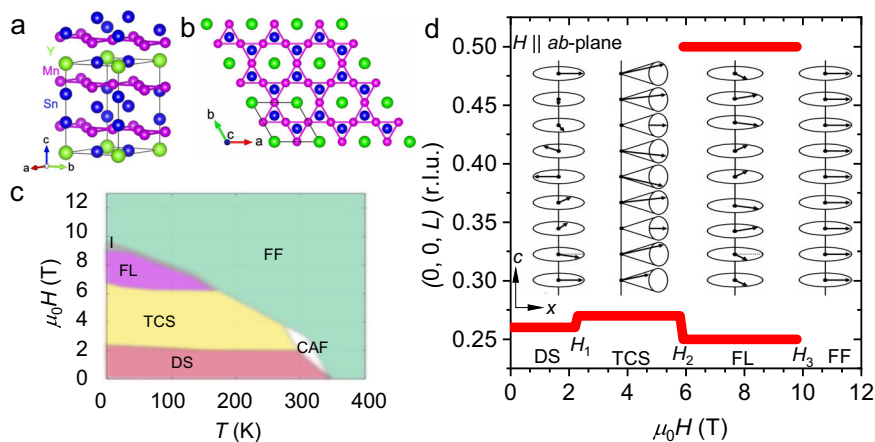


Fig. 1 Crystal structure and magnetic properties of YMn_6Sn_6 . **a** Crystal structure of YMn_6Sn_6 . **b** c -axis view of the structure showing Mn atoms arranged in a kagome-net in the ab -plane. **c** Schematic temperature (T) and magnetic field (H) phase diagram of YMn_6Sn_6 labeled for the various magnetic phases for field applied in the ab -plane including the distorted spiral (DS), transverse conical spiral (TCS), fan-like (FL), and forced ferromagnetic (FF) phases. Small pockets labeled as I and CAF represent phase I and the canted antiferromagnetic phase, respectively. **d** Plot of the wavevector ($L = k_z$) of the magnetic Bragg peaks observed in neutron diffraction experiments at 10 K (red lines) and illustrations of the magnetic structures for DS, TCS, FL, and FF phases. Magnetic fields at which transitions from DS to TCS, TCS to FL, and FL to FF are indicated by H_1 , H_2 , and H_3 , respectively. Arrows represent the direction of spins in each Mn-layer. The labels c and x represent c -axis and the direction of magnetic field in the ab -plane, respectively.

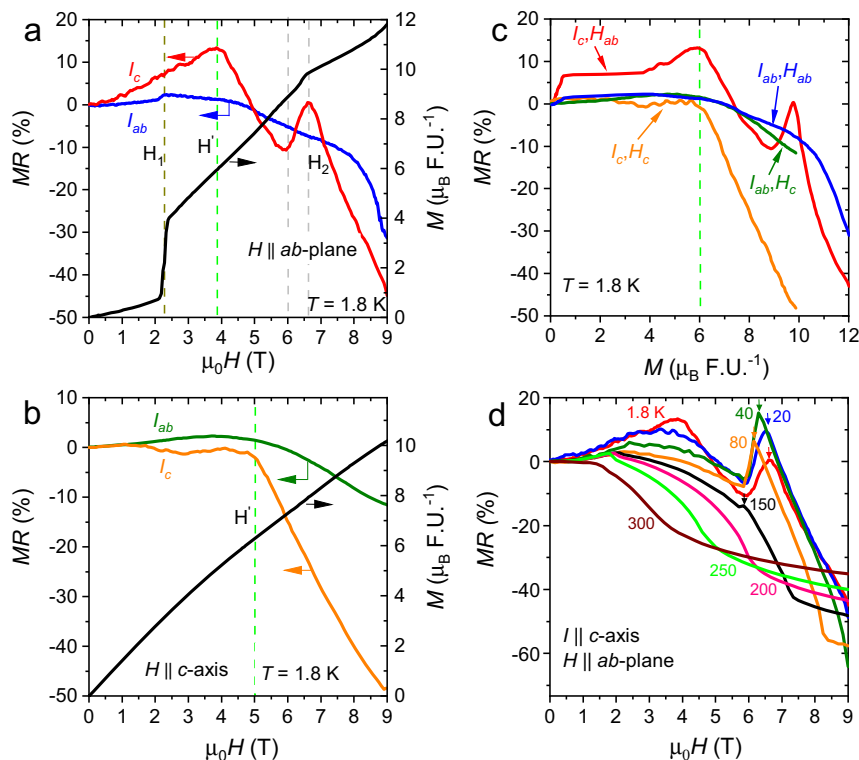


Fig. 2 Magnetoconductance, and magnetization of YMn_2Sn_6 . **a, b** Magnetoconductance (MR) at 1.8 K for current along the c -axis, I_c , and in the ab -plane, I_{ab} , and the magnetization, M , as a function of magnetic field, H . H is applied in the ab -plane in panel (a), and along the c -axis in panel (b). Dark gray dashed lines indicate transitions from the distorted spiral to transverse conical spiral phase (H_1) and light gray dashed lines indicate the transition from transverse conical spiral to fan-like phase (H_2). Green dashed lines corresponds to the MR turnover (H'). **c** MR as a function of M at 1.8 K. The symbols H_c and H_{ab} refer to the magnetic field applied along the c -axis and in the ab -plane, respectively. Green dashed line shows the MR turnover at H' occurs at $6 \mu_B \text{F.U.}^{-1}$ independent of applied field direction. Demagnetization considerations are discussed in Supplementary Note 1. **d** MR for I_c and H_{ab} at the indicated temperatures. The arrows track the MR peak at H_2 .

magnetization. Second, MR_{I_c} drops sharply at 4 T with no corresponding change in magnetization. Third, it again increases sharply, by about 10% at 6 T, peaks at H_2 , and then again drops sharply.

MR and magnetization with the magnetic field along the c -axis are presented in Fig. 2b. Here, the magnetization smoothly increases up to 9 T indicating a continuous canting of the spins towards the c -axis. MR for current in the ab -plane ($\text{MR}_{I_{ab}}$) (green) initially increases, reaching a maximum at 4.5 T and then decreases with a smaller overall change ($\sim 8\%$) in MR. The drop for MR with the current applied along the c -axis MR_{I_c} (orange) is much larger (45%) beginning at 5 T. We refer to this magnetic field, where MR drops without a corresponding change in magnetization, as H' .

In Fig. 2c, the MRs measured in all four configurations at 1.8 K are plotted together as a function of the corresponding magnetic moment. The plot shows that the H' MR drop occurs, irrespective of orientation, when the magnetization reaches $6 \mu_B \text{F.U.}^{-1}$, indicating that the H' MR drop is magnetization induced. The highly anisotropic nature of this H' feature, indicated by a larger change for current along the c -axis than in the ab -plane, suggests that the electronic state driving it is highly anisotropic. It is to be noted that the small jump in MR_{I_c} with field in the ab -plane (red curve) at $1 \mu_B \text{F.U.}^{-1}$ of M is related to the sudden increase in M at H_1 . The temperature evolution of the MR_{I_c} for the in-plane field is depicted in Fig. 2d for selected temperatures. The full temperature range measured for each of the current and applied field configurations is discussed in Supplementary Note 4. The H'

drop in MR starts broadening at 20 K and disappears above 40 K. A typical reason for a drop in magnetoconductance (or negative magnetoconductance) is suppression of spin fluctuations by the magnetic field. However, in our case several experimental observations preclude such an explanation for the H' -MR drop. First, the negative MR related to suppression of spin fluctuation should be more pronounced closer to the transition temperature, while it is exactly the opposite in our case. Second, the H' -MR drop is highly anisotropic with respect to the in- and out-of plane currents, but the H' -MR signature occurs exactly when the magnetization reaches $6 \mu_B \text{F.U.}^{-1}$, regardless of the direction of the applied magnetic field, and despite the fact that the magnetic fields along c -axis and in the ab -plane stabilize different magnetic structures: gradual spin canting towards the c -axis, and a transverse conical spiral, respectively. Third, thermal conductivity measured as a function of temperature peaks at 38 K and sharply decreases below this temperature (see Supplementary Note 5), suggesting that the phonons are being frozen out below 38 K, leaving the electronic contribution to the thermal conductivity as the primary source of heat transport. This behavior matches with the temperature dependence of the H' -MR drop that disappears above 40 K due to thermal activation of phonons and increased phonon scattering. The H_2 MR peak follows the fan-like phase shown in the phase diagram in Fig. 1c. The peak persists to 150 K and disappears by 200 K, matching with the fan-like phase boundary at 170 K¹⁰.

Thus, we conclude that the observed MR features are triggered by some changes in the electronic structure. In order to relate those to the microscopic magnetic structure, we plot the 1.8-K

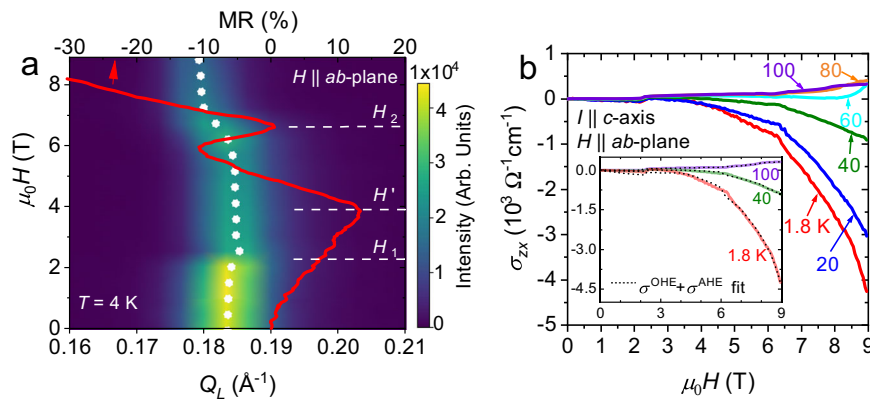


Fig. 3 Magnetotransport and small angle neutron scattering intensity of YMn_6Sn_6 . **a** Neutron intensity-Q map of the magnetic field dependence of the magnetic Bragg peak observed in small angle neutron scattering, adapted from Ghimire, et al.^{10, 20}, plotted together with the magnetoresistance (MR) for current along the c -axis. Q_L refers to the z -component of the scattering vector, Q . In both cases, magnetic field is applied in the ab -plane. The white dots are a guide to the peak center. White dashed lines locate the magnetic structure transitions indicated by H_1 and H_2 and the MR turnover at H' . **b** Hall conductivity, σ_{zx} , as a function of magnetic field, H , at indicated temperatures. Inset depicts the fits (black dotted lines) of the Hall conductivity comprised of only ordinary, $\sigma^{\text{OHE}} = R_H H \rho_{zz}^{-1} \rho_{xx}^{-1}$, and anomalous, $\sigma^{\text{AHE}} = S_H M$, conductivity contributions, where R_H is the ordinary Hall coefficient, and S_H is the anomalous Hall coefficient, M is the magnetization vs field applied in the ab -plane, and ρ_{zz} and ρ_{xx} are the longitudinal resistivities for current applied along the c -axis and current applied in the ab -plane, respectively.

MR_c for the in-plane magnetic field together with the magnetic Bragg peak measured using small angle neutron scattering at 4 K in Fig. 3a. The intensity of the Bragg peak does not show a noticeable change below H_1 . At H_1 , the Bragg peak loses intensity and the wavevector slightly increases marking the distorted spiral - transverse conical spiral phase transition. There is no apparent change in the intensity or the wavevector at H' , the MR turnover field, signifying no change in magnetic structure at H' besides a gradual spin canting. The H_2 peak in MR corresponds exactly to the region where the wavevector of the magnetic Bragg peak changes at the transverse conical spiral to fan-like phase boundary. Once in the fan-like phase, the MR starts decreasing as the magnetic field starts canting the spins along the field. These observations unambiguously show that the H' MR drop and H_2 MR peak are associated with the magnetic field induced changes in the electronic and magnetic structures, respectively, with the former being magnetization driven indicating an LT. An LT is usually accompanied by a change in carrier concentration observable through Hall effect measurements. However, we do not see a noticeable slope change in the Hall conductivity (Fig. 3b) or resistivity (Supplementary Fig. 9) at H' , but rather a gradual change. This paradox can be related to the complex fermiology of a metal with a complicated band structure (see Supplementary Note 6). Note that while magnetoresistance and Hall conductivity are closely related, a 10% change (the immediate change at H') in the former does not necessarily correspond to a measurable change in the latter, especially when it is dominated by the anomalous term, as in this case (see Supplementary Note 7).

Microscopic origin of magnetoresistance signatures. To investigate the microscopic origin of the LT, we calculated the non-relativistic electronic band structure in the experimental zero-field zero-temperature spiral magnetic phase and in the fully polarized ferromagnetic state. Ferromagnetic band structure calculations suggested that the effect of SOC on the band dispersions is, expectedly, rather weak in YMn_6Sn_6 , so most of the reported calculations were performed without SOC. In the zero-field state (blue bands), there are no bands at the Fermi energy (E_F) at the L -point as depicted in Fig. 4a. On the contrary, in the polarized

state, a flat band from the spin majority channel appears at E_F , emphasized in bold in Fig. 4a. It forms a highly anisotropic hole pocket around L , visible as a pancake shape in Fig. 4b, where the Fermi surface for the spin majority bands is depicted. This hole pocket is highly dispersive along c , nearly flat in the $L-A$ direction and rather heavy along $L-H$. Due to its quasi-1D nature, this hole pocket contributes mainly to the transport along c . Other features of the Fermi surface include one large electron pocket around H and one large hole pocket around K , forming two networks of interconnected triangular pillows. These pockets are also more dispersive along c , but are much less anisotropic than the hole pocket around L . In addition, there are also two small electron pockets: one between L and M , a remnant of a quasi-2D band, and another around Γ . Overall, somewhat counterintuitively for the layered structure of YMn_6Sn_6 , the spin-up electrons propagate more easily perpendicular to the Mn planes. Spin-down bands, on the contrary, prefer the in-plane transport. It can be inferred that the new Fermi surface appears, via an LT, well below full saturation, i.e., when the moments attain a value of $M = 6\mu_B \text{F.U.}^{-1}$ at H' , and is responsible for the sharp drop in MR. This is consistent with the fact that the drop occurs at different field magnitudes for the in-plane and out-of-plane field directions, but at the same M , and is considerably more pronounced for the c -axis MR. We emphasize that the electronic structure is sensitive to the direction of the spin polarization only as much as the SOC (tens of meV) is strong compared to the non-relativistic electron energy (eVs). Thus in a material with a weak SOC, such as this compound, the change in the Fermi surface occurs independent of the direction of polarization, as observed in the H' -MR drop occurring when the moments attain a value of $M = 6\mu_B \text{F.U.}^{-1}$, regardless of the direction of spin polarization.

Turning attention to the H_2 -MR peak that occurs during the transverse conical spiral to fan-like phase transition, we calculate the hopping probabilities (which in turn determine the conductivities) in each of the phases within a tight-binding approximation. For a 1D chain, the probability for an electron to travel along the chain is determined by the lowest of the individual probabilities which we call the bottleneck. The hopping between two electrons with non-parallel spins is proportional to half of the cosine of the angles between them. The experimentally

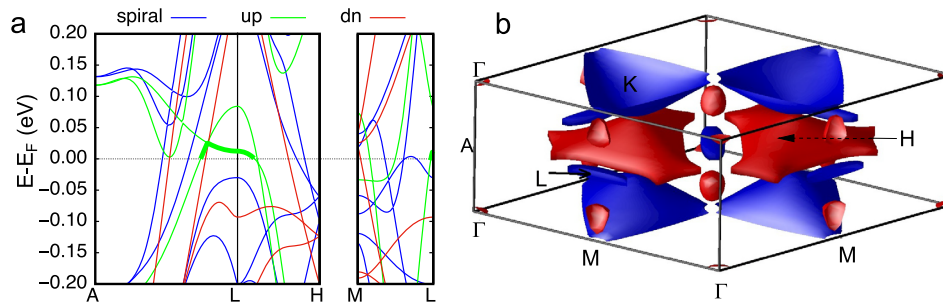


Fig. 4 Electronic band structure and Fermi surface of YMn_6Sn_6 . **a** Calculated electronic band structure near the Fermi energy, E_F , at the L point of YMn_6Sn_6 in the magnetic spiral ground state, (blue lines) and in the spin polarized state. The lines with green, and red color represent spin up (up) and spin down (dn) bands, respectively. All calculated bands are shown in Supplementary Fig. 8. **b** Calculated Fermi surface around Γ , M and L points.

determined largest angles between two spins in the transverse conical spiral and fan-like phases are 67.9° , and 81° , respectively¹¹ [see Supplementary Note 8 for details]. Thus, the bottleneck factor in the transverse conical spiral and fan-like phases for the c -axis transport is 0.83, and 0.76, respectively. The bottleneck factor along c (but not in-plane) in the transverse conical spiral phase is 9% higher than that in the fan-like phase, quantitatively accounting for the 10% rise of the interplaner magnetoresistance. It is to be noted here that this effect is entirely due to the spin texture and not to the SOC, as evidenced by a negligible MR for a much larger magnetization change at H_1 . Such an interplaner MR has been discussed with respect to the chiral soliton lattice phase in $Cr_{1/3}NbS_2$ ¹³, where the Dzyaloshinskii-Moriya interaction driven chirality is inherently coupled to the SOC. The charge-spin coupling in YMn_6Sn_6 is unique in that it requires neither chirality nor a strong SOC.

Common LTs, driven by doping, strain, or pressure, are often associated with van Hove singularities¹⁴ that are difficult to observe via transport measurements. Moreover, those LTs are rather inflexible, since chemical doping cannot be controlled in situ within the same sample, and varying strain or pressure appreciably is difficult. An uncommon magnetization driven LT is free of these shortcomings, and has potential as a tool to tune the FS topology. We emphasize that while this specific LT is rather fortuitous, considerable modification of the FS via applied field in spiral magnets is to be expected, and it is likely that similar LTs will be discovered in other spiral magnets. The magnetic transition at H_2 , which occurs between two ordered phases, as opposed to the spin-flop transition at H_1 , does affect the MR (but only along c), as shown in Fig. 2a. The scale of this effect can be estimated from the standard formula relating the one-electron hopping probability to the angle between the local magnetic moments¹⁵ and is consistent with the experimental change in MR. This behavior marks the electron-spin interaction without the requirement of strong SOC or spin chirality, as in the chiral magnets^{13, 16}.

Conclusions

In summary, our magnetotransport measurements in varying applied magnetic fields, and in different current directions, uncover two nontrivial effects in magnetoresistance. Using first-principles calculations, we were able to identify one of them, which occurs at a magnetization of $M = 6\mu_B F.U.^{-1}$ for any field direction, as a magnetization driven Lifshitz transition, qualitatively different from common pressure or strain driven ones. The other effect demonstrates how magnetotransport phenomena are intimately related to the change in magnetic texture. These types of effects are strongly desired for potential spintronic applications and, thus, our results provide a compelling observation to

stimulate new theoretical and experimental research into the interaction between the topology of electronic bands in kagome lattices, magnetic interactions, and spin-orbit coupling, especially in the rare-earth ternary kagome magnet systems.

Methods

Single crystal growth. Single crystals of YMn_6Sn_6 were grown by the self-flux method. Y pieces (Alfa Aesar; 99.9%), Mn pieces (Alfa Aesar; 99.95%), and Sn shots (Alfa Aesar; 99.999%) were loaded in a 2-ml aluminum oxide crucible in a molar ratio of 1:1:20. The crucible was sealed in a fused silica ampoule under vacuum and heated to $1175^\circ C$ over 10 h, homogenized at $1175^\circ C$ for 12 h, and then cooled to $600^\circ C$ over 100 h. Upon reaching $600^\circ C$ the excess flux was decanted from the crystals using a centrifuge leaving behind well-faceted hexagonal crystals up to 100 mg in mass. All measurements were performed on crystals oriented for the $[0, 0, 1]$ and $[1, 1, 0]$ directions.

Transport and magnetization. For electrical transport measurements samples were polished to dimensions of $\sim 1.00 \times 0.40 \times 0.15$ mm with the long axis corresponding to either the c -axis, or the in-plane, $[1, 1, 0]$, direction. An excitation current of 4 mA was used in all measurements presented. Identical data were also measured with a 2 mA excitation, however, the higher 4 mA current produced less noise without impacting the features observed. Electrical contacts were affixed using Epotek H20E silver epoxy and 25 μm Pt wires with typical contact resistances of $\approx 20 \Omega$, such that current was directed along the c -axis or in the ab -plane. MR and Hall effect data were collected using the resistivity option and rotator within a Quantum Design DynaCool PPMS equipped with a 9 T magnet. MR is defined as $MR = (\rho(H) - \rho(0))/\rho(0)$, where $\rho(H)$ and $\rho(0)$ are the longitudinal resistivity with and without an applied magnetic field, H . The Hall resistivity was asymmetric from the positive and negative applied magnetic fields via $\rho_{xz} = [\rho_T(+H) - \rho_T(-H)]/2$, where ρ_T is the resistivity measured via the transverse voltage contacts in the Hall bar geometry. Hall conductivity for current along the c -axis was calculated via the relation $\sigma_{xx} = \rho_{xz}/(\rho_{xz}^2 + \rho_{zz}\rho_{xx})$. Here, ρ_{zz} is the longitudinal resistivity for current along the c -axis and magnetic field in the ab -plane, ρ_{xx} is the longitudinal resistivity for mutually perpendicular current and magnetic field in the ab -plane, and ρ_{zx} is the Hall resistivity for current along c . It is to be noted that the $\rho_{zz}\rho_{xx}$ term in the denominator is due to the anisotropy in ρ_{xx} and ρ_{zz} in the hexagonal system as evident in Supplementary Fig. 4. The fits of the Hall conductivity were piecewise above and below H_2 , where the transverse conical spiral to fan-like transition imparts a significant change to the electronic structure and hence the Hall conductivity. DC magnetization measurements were performed in the same PPMS system using the ACMS II option.

Small angle neutron scattering. Small Angle Neutron Scattering data were collected with the NG-7 SANS instrument at the NIST Center for Neutron Research using a 9 T horizontal field magnet ($H||[1, 1, 0]$) and in the temperature range from 4 K to 300 K. For Fig. 3a, conversion of wavevector to \AA^{-1} from r.l.u units is made through the following relation, $Q_L(\text{\AA}^{-1}) = 2\pi L/c$, where L is the z -component of the wavevector in r.l.u. [$k = (H, K, L)$], and c is the c -axis unit vector length in \AA .

First-principles calculations. Most calculations were performed using the projected augmented wave pseudo-potential code VASP¹⁷ and the gradient-dependent density functional of Perdew, et al.¹⁸ For control purposes, some calculations were also repeated using the all-electron linearized augmented plane wave code WIEN2k¹⁹.

Data availability

The authors declare that the main data supporting the findings of this study are available within the article and its Supplementary Information files. Extra data are available from the corresponding author upon request.

Received: 22 November 2021; Accepted: 14 February 2022;

Published online: 15 March 2022

References

- Lifshitz, I. M. Anomalies of electron characteristics of a metal in the high pressure region. *Sov. Phys. JETP* **11**, 1130–1135 (1960).
- Volovik, G. E. Exotic Lifshitz transitions in topological materials. *Phys.-Uspekhi* **61**, 89 (2018).
- Okada, Y. et al. Observation of Dirac Node formation and mass acquisition in a topological crystalline insulator. *Science* **27**, 1496–1499 (2013).
- Zeljko, I. et al. Mapping the unconventional orbital texture in topological crystalline insulators. *Nat. Phys.* **10**, 572–577 (2014).
- Kitaori, A. et al. Emergent electromagnetic induction beyond room temperature. *Proc. Natl Acad. Sci.* **118**, e2105422118 (2021).
- Li, M. et al. Dirac cone, flat band and saddle point in kagome magnet YMn_6Sn_6 . *Nat. Commun.* **12**, 1–8 (2021).
- Yin, J. X. et al. Quantum-limit Chern topological magnetism in TbMn_6Sn_6 . *Nature* **583**, 533–536 (2020).
- Zhang, H. et al. Topological magnon bands in a room-temperature kagome magnet. *Phys. Rev. B* **101**, 100405 (2020).
- Mazet T. et al. A study of the new HfFe_6Ge_6 -type ZrMn_6Sn_6 and HfMn_6Sn_6 compounds by magnetization and neutron diffraction measurements. *J Alloys Comp.* **284**, 54–59 (1999).
- Ghimire, N. J. et al. Competing magnetic phases and fluctuation-driven scalar spin chirality in the kagome metal YMn_6Sn_6 . *Sci. Adv.* **6**, eabe2680 (2020).
- Dally, R. L. et al. Chiral properties of the zero-field spiral state and field-induced magnetic phases of the itinerant kagome metal YMn_6Sn_6 . *Phys. Rev. B* **103**, 094413 (2021).
- Wang, Q. et al. Field-induced topological Hall effect and double-fan spin structure with a c -axis component in the metallic kagome antiferromagnetic compound YMn_6Sn_6 . *Phys. Rev. B* **103**, 014416 (2021).
- Togawa, Y. et al. Interlayer magnetoresistance due to chiral soliton lattice formation in hexagonal chiral magnet CrNb_3S_6 . *Phys. Rev. Lett.* **111**, 197204 (2013).
- Sunko, V. et al. Direct observation of uniaxial stress-driven Lifshitz transition in Sr_2RuO_4 . *npj Quantum Mater.* **4**, 1–7 (2019).
- Khomskii, D. I. *Basic Aspects of the Quantum Theory of Solids: Order and Elementary Excitations*. Cambridge University Press (2010).
- Neubauer, A. et al. Topological Hall Effect in the A Phase of MnSi . *Phys. Rev. Lett.* **102**, 186602 (2009).
- Kresse, G. & Furthmüller, J. Efficient iterative schemes for ab initio total-energy calculations using a plane-wave basis set. *Phys. Rev. B* **54**, 11169 (1996).
- Perdew, J. P., Burke, K. & Ernzerhof, M. Generalized gradient approximation made simple. *Phys. Rev. Lett.* **77**, 3865 (1996).
- Blaha, P. et al. *An augmented plane wave plus local orbitals program for calculating crystal properties*. Vienna University of Technology (2001).
- Figure adapted from Ghimire et al. *Science Advances*, 18 Dec 2020, Vol 6, Issue 51, DOI: 10.1126/sciadv.abe2680. © the Authors, some rights reserved; exclusive licensee AAAS. Distributed under a CC BY-NC 4.0 license <http://creativecommons.org/licenses/by-nc/4.0/>.

Acknowledgements

Crystal growth and properties characterization work at George Mason University was supported by the U.S. Department of Energy, Office of Science, Basic Energy Sciences, Materials Science and Engineering Division. I.I.M. acknowledges support from the U.S. Department of Energy through the grant #DE-SC0021089. M.P.G. acknowledges the Alexander von Humboldt Foundation, Germany for the equipment grants. Access to the NG-7 SANS instrument was provided by the Center for High Resolution Neutron Scattering, a partnership between the National Institute of Standards and Technology and the National Science Foundation under Agreement No. DMR-2010792. The identification of any commercial product or trade name does not imply endorsement or recommendation by the National Institute of Standards and Technology. We thank J.F. Mitchell for useful discussions.

Author contributions

N.J.G. and P.E.S. conceived the idea. P.E.S. performed magnetic and magnetotransport measurement and carried out the data analysis. H.B. synthesized single crystals. D.C.J. contributed to the figure preparation. R.L.D., L.P. and J.W.L. contributed to neutron diffraction experiments. L.P., N.J.G., J.W.L. and M.B. performed SANS experiment. I.I.M. and M.P.G. contributed to the DFT calculations. P.E.S. and N.J.G. wrote the manuscript. All authors contributed to the discussion of the results.

Competing interests

The authors declare no competing interests.

Additional information

Supplementary information The online version contains supplementary material available at <https://doi.org/10.1038/s42005-022-00833-2>.

Correspondence and requests for materials should be addressed to Peter E. Siegfried or Nirmal J. Ghimire.

Peer review information *Communications Physics* thanks Shuang Jia and the other, anonymous, reviewer(s) for their contribution to the peer review of this work.

Reprints and permission information is available at <http://www.nature.com/reprints>

Publisher's note Springer Nature remains neutral with regard to jurisdictional claims in published maps and institutional affiliations.



Open Access This article is licensed under a Creative Commons Attribution 4.0 International License, which permits use, sharing, adaptation, distribution and reproduction in any medium or format, as long as you give appropriate credit to the original author(s) and the source, provide a link to the Creative Commons license, and indicate if changes were made. The images or other third party material in this article are included in the article's Creative Commons license, unless indicated otherwise in a credit line to the material. If material is not included in the article's Creative Commons license and your intended use is not permitted by statutory regulation or exceeds the permitted use, you will need to obtain permission directly from the copyright holder. To view a copy of this license, visit <http://creativecommons.org/licenses/by/4.0/>.

© The Author(s) 2022